Key Points:
- Obliquity of EMIC waves can reduce the scattering efficiency
- EMIC wave scattering can cause the top-hot electron distribution
- Different EMIC bands are important for RB electrons at different energies

Correspondence to:
B. Ni,
bbni@whu.edu.cn

Resonant scattering of outer zone relativistic electrons by multiband EMIC waves and resultant electron loss time scales

Binbin Ni[1], Xing Cao[1], Zhengyang Zou[1], Chen Zhou[1], Xudong Gu[1], Jacob Bortnik[2], Jichun Zhang[3], Song Fu[1], Zhengyu Zhao[1], Run Shi[4], and Lun Xie[5]

[1]Department of Space Physics, School of Electronic Information, Wuhan University, Wuhan, China, [2]Department of Atmospheric and Oceanic Sciences, University of California, Los Angeles, California, USA, [3]Space Science Center and Department of Physics, University of New Hampshire, Durham, New Hampshire, USA, [4]Department of Mathematics and Statistics, Memorial University of Newfoundland, St. John's, Newfoundland, Canada, [5]Institute of Space Physics and Applied Technology, Peking University, Beijing, China

Abstract To improve our understanding of the role of electromagnetic ion cyclotron (EMIC) waves in radiation belt electron dynamics, we perform a comprehensive analysis of EMIC wave-induced resonant scattering of outer zone relativistic (>0.5 MeV) electrons and resultant electron loss time scales with respect to EMIC wave band, L shell, and wave normal angle model. The results demonstrate that while H$^+$-band EMIC waves dominate the scattering losses of ~1–4 MeV outer zone relativistic electrons, it is He$^+$-band and O$^+$-band waves that prevail over the pitch angle diffusion of ultrarelativistic electrons at higher energies. Given the wave amplitude, EMIC waves at higher L shells tend to resonantly interact with a larger population of outer zone relativistic electrons and drive their pitch angle scattering more efficiently. Obliquity of EMIC waves can reduce the efficiency of wave-induced relativistic electron pitch angle scattering. Compared to the frequently adopted parallel or quasi-parallel model, use of the latitudinally varying wave normal angle model produces the largest decrease in H$^+$-band EMIC wave scattering rates at pitch angles $< $ ~40° for electrons $> $ ~5 MeV. At a representative nominal amplitude of 1 nT, EMIC wave scattering produces the equilibrium state (i.e., the lowest normal mode under which electrons at the same energy but different pitch angles decay exponentially on the same time scale) of outer belt relativistic electrons within several to tens of minutes and the following exponential decay extending to higher pitch angles on time scales from $<$1 min to ~1 h. The electron loss cone can be either empty as a result of the weak diffusion or heavily/fully filled due to approaching the strong diffusion limit, while the trapped electron population at high pitch angles close to 90° remains intact because of no resonant scattering. In this manner, EMIC wave scattering has the potential to deepen the anisotropic distribution of outer zone relativistic electrons by reshaping their pitch angle profiles to "top-hat." Overall, H$^+$-band and He$^+$-band EMIC waves are most efficient in producing the pitch angle scattering loss of relativistic electrons at ~1–2 MeV. In contrast, the presence of O$^+$-band EMIC waves, while at a smaller occurrence rate, can dominate the scattering loss of 5–10 MeV electrons in the entire region of the outer zone, which should be considered in future modeling of the outer zone relativistic electron dynamics.

1. Introduction

Propagating at frequencies below the proton gyrofrequency (f_{cp}), electromagnetic ion cyclotron (EMIC) waves have been extensively observed in the inner magnetosphere in the frequency range 0.1–5.0 Hz, i.e., the ultralow frequency Pc1–2 band [e.g., *Anderson et al.*, 1992a, 1992b; *Fraser et al.*, 1992, 1996; *Fraser and Nguyen*, 2001; *Meredith et al.*, 2003, 2014; *Zhang et al.*, 2014]. Partially controlled by the ion composition and anisotropy [e.g., *Kozyra et al.*, 1984; *Horne and Thorne*, 1994] and by the location with respect to the plasmapause [*Fraser and Nguyen*, 2001], EMIC waves can be generated in three distinct frequency bands below the hydrogen (H$^+$), helium (He$^+$), and oxygen (O$^+$) ion gyrofrequencies. Compared to the frequently measured H$^+$-band and He$^+$-band EMIC waves, O$^+$-band EMIC waves are rarely observed but were recently reported in the outer plasmasphere at L = 2–5 from the Van Allen Probes Electric and Magnetic Field Instrument Suite and Integrated Science and Electric Fields and Waves data [*Yu et al.*, 2015].

While EMIC waves are present during geomagnetically quiet periods, their occurrence and intensity increases during disturbed geomagnetic conditions [*Bräysy et al.*, 1998; *Erlandson and Ukhorskiy*, 2001;

Meredith et al., 2014]. Observed over a broad range of L shell from L = 3 to L = 10, EMIC waves have typical amplitudes in the range of ~0.1–10 nT [*Fraser et al.*, 1996; *Erlandson and Ukhorskiy*, 2001]. These waves occur characteristically over a broad range of magnetic local time (MLT) from the postnoon to dawnside, approximately 14:00–07:00 MLT, with the maximum of occurrence probability in the afternoon sector [e.g., *Meredith et al.*, 2003; *Min et al.*, 2012]. Using the Active Magnetospheric Particle Tracer Explorers (AMPTE) Charge Composition Explorer data, *Anderson et al.* [1992a] reported that the occurrence rate of EMIC waves increases monotonically with L in the region L = 3–9, peaking at 10%–20% in the spatial region at 11:00–15:00 MLT within L = 7–9. Analyzing the Time History of Events and Macroscale Interactions Flux Gate Magnetometer data with an automated EMIC Pc1 wave detection algorithm, *Usanova et al.* [2012] found that, in general, the EMIC wave occurrence rate increases with L in the dawn, noon, dusk, and midnight sectors, showing the highest occurrence rate (5%–8%) in the noon and dusk sectors and reaching its maximum at L~9 (see Figure 4 of *Usanova et al.* [2012]). Such an MLT dependence of EMIC wave occurrence is consistent with the westward drift of energetic ions, which are commonly regarded as the free-energy source population for EMIC wave excitation. More recently, *Meredith et al.* [2014], by performing a statistical analysis of EMIC waves observed by CRRES, found that the average intensity of H^+-band and He^+-band EMIC waves in the region $L^* = 4$–7 (where L^* is the Roederer parameter related to the third adiabatic invariant [*Roederer*, 1970]) in the afternoon sector under actively disturbed conditions is $0.5\,nT^2$ and $2\,nT^2$, respectively. While H^+-band EMIC waves are most common in the outer magnetosphere (L = 7–9) on the afternoon side regardless of geomagnetic activity, He^+-band EMIC waves occur most frequently in the inner magnetosphere (L = 4–7) on the prenoon to dusk side during active times [*Keika et al.*, 2013].

Primarily generated by the anisotropic distribution of 1–100 keV ring current protons that are formed by the earthward ion convection from the magnetotail during geomagnetically disturbed periods [e.g., *Cornwall et al.*, 1970; *Jordanova et al.*, 2001; *Zhang et al.*, 2014], EMIC waves preferentially occur in regions of high density either localized along the duskside plasmapause [e.g., *Pickett et al.*, 2010] or within dayside drainage plumes [e.g., *Morley et al.*, 2009]. The compression of the magnetopause is suggested as another possible source of EMIC waves [e.g., *Anderson and Hamilton*, 1993; *McCollough et al.*, 2012; *Usanova et al.*, 2008]. While it is frequently thought that EMIC emissions are generated along the field line at the equatorial source region particularly in the inner magnetosphere, information about the wave normal angle of EMIC waves is very limited. *Anderson et al.* [1992b] showed that near the equator the waves are a mixture ranging from left hand circularly polarized waves to highly elliptical or linearly polarized waves, while at higher latitudes the waves become more linearly polarized. Such wave properties suggest that EMIC emissions can deviate from parallel or quasi-parallel propagation after generation and become more oblique as they propagate to higher latitudes [*Horne and Thorne*, 1994].

The importance of EMIC waves to magnetospheric particle dynamics has been long recognized, since they are capable of causing thermal plasma heating [e.g., *Thorne and Horne*, 1992, 1997; *Zhang et al.*, 2010, 2011] and also driving losses of both ring current protons [e.g., *Cornwall et al.*, 1970; *Summers*, 2005; *Liang et al.*, 2014] and relativistic electrons [e.g., *Thorne and Kennel*, 1971; *Summers and Thorne*, 2003; *Summers et al.*, 2007; *Ma et al.*, 2015] via resonant pitch angle scattering. While evident connections between pitch angle scattering by EMIC waves and relativistic electron loss processes have been established from a number of observations [e.g., *Clilverd et al.*, 2007; *Miyoshi et al.*, 2008; *Rodger et al.*, 2008; *Usanova et al.*, 2014], accurate quantification of the effects of EMIC wave-driven electron diffusion is complex. It requires not only detailed information of the background magnetic field and ambient plasma density but also reliable wave properties including average root-mean-square amplitude, frequency spectrum, wave normal angle distribution, and latitudinal coverage. Compared to the other parameters, the wave normal angle information during the propagation of EMIC waves is difficult to acquire directly from in situ observations. Although EMIC waves are believed to become more and more oblique during their propagation to higher latitudes mainly due to the geomagnetic field gradient and curvature, previous studies have commonly adopted a parallel or quasi-parallel propagation assumption to determine the resonant scattering rates of EMIC waves [e.g., *Summers and Thorne*, 2003; *Summers*, 2005; *Summers et al.*, 2007; *Li et al.*, 2007; *Ukhorskiy et al.*, 2010; *Subbotin et al.*, 2010; *Kersten et al.*, 2014; *Ma et al.*, 2015]. The major purpose of this study is to evaluate the quantitative role of EMIC waves in driving scattering loss of outer radiation belt relativistic electrons and its sensitivity to wave normal angle distribution. In addition, besides H^+-band and He^+-band EMIC waves, the scattering effect of O^+-band EMIC waves deserves a comprehensive investigation as well, since this wave mode also occurs occasionally in the outer zone [e.g., *Fraser et al.*, 1992; *Yu et al.*, 2015].

The outline of this paper is as follows. In section 2, we give a brief description of the adopted models for the background magnetic field and plasma density and for the three bands (H^+, He^+, and O^+) of EMIC waves. We also briefly describe the code used to quantify the quasi-linear bounce averaged pitch angle diffusion coefficients. Computed results of EMIC wave-driven relativistic electron scattering rates and loss cone filling index, corresponding to different EMIC wave bands, L shells, and wave normal angle models, are displayed in section 3. We show the numerical results of pure pitch angle diffusion modeling and resultant electron loss time scales due to EMIC waves in section 4, which is followed by discussions in section 5 and conclusions in section 6.

2. Model Description

To model EMIC waves, we first assume that the three wave bands all follow a Gaussian frequency distribution, taking the form [e.g., *Glauert and Horne*, 2005; *Meredith et al.*, 2014; *Kersten et al.*, 2014]

$$I_B(\omega) = A \exp\left[-\left(\frac{\omega - \omega_m}{\delta\omega}\right)^2\right] (\omega_{lc} \leq \omega \leq \omega_{uc}), \qquad (1)$$

where I_B is the power spectral intensity of the wave magnetic field (in pT^2/Hz); ω_m and $\delta\omega$ are the frequency of maximum wave power and bandwidth, respectively; ω_{lc} and ω_{uc} are the lower and upper cutoffs to the wave spectrum outside, in which the wave power is zero, and A is a normalization factor given by

$$A = \frac{B_w^2}{\delta\omega} \frac{2}{\pi^{1/2}} \left[\text{erf}\left(\frac{\omega_m - \omega_{lc}}{\delta\omega}\right) + \text{erf}\left(\frac{\omega_{uc} - \omega_m}{\delta\omega}\right)\right]^{-1}, \qquad (2)$$

where B_w is the wave magnetic field amplitude in units of nT and erf is the error function. The wave normal distribution of EMIC waves is also assumed to be Gaussian and given by [e.g., *Glauert and Horne*, 2005; *Ni et al.*, 2013, 2014a, 2014b; *Kersten et al.*, 2014]

$$g(\theta) = \exp\left[-\left(\frac{\tan\theta - \tan\theta_m}{\tan\theta_w}\right)^2\right] (\theta_{lc} \leq \theta \leq \theta_{uc}), \qquad (3)$$

where θ is the wave normal angle, θ_m is the wave angle with peak power, θ_w is the angular width, and θ_{lc} and θ_{uc} are the lower and upper bounds to the wave normal distribution outside, in which the wave power is zero.

The present study focuses on the outer radiation belt with a spatial coverage of L = 3–7, for which a dipole geomagnetic field model is adopted. Since EMIC waves preferentially occur in the high-density regions overlapping with the hot anisotropic ions, we obtain the equatorial plasma density (N_0) values by using the plasmaspheric density model of *Sheeley et al.* [2001] as follows:

$$N_0 = 1390(3/L)^{4.83} \text{ cm}^{-3}, \qquad (4)$$

and assume that the plasma density does not change with magnetic latitude along the field line. Taking into account the effect of the ion concentration, we perform the investigation in a cold, multi-ion (H^+, He^+, and O^+) plasma defined by the ratio of each ion, say, $\rho_1 = n_1/N_0$, $\rho_2 = n_2/N_0$, and $\rho_3 = n_3/N_0$, where n_1, n_2, and n_3 denote the hydrogen (H^+), helium (He^+), and oxygen (O^+) ion number densities, respectively.

Specifically, for the spatial extent of L = 3–7 of interest, we follow the previous studies [e.g., *Summers and Thorne*, 2003; *Summers et al.*, 2007] and use the representative parameters below for each wave band: (1) H^+ band: $\omega_{lc} = 0.5\Omega_1$, $\omega_{uc} = 0.7\Omega_1$, $\omega_m = 0.6\Omega_1$, $\delta\omega = 0.1\Omega_1$, $\rho_1 = 0.85$, $\rho_2 = 0.1$, and $\rho_3 = 0.05$, where Ω_1 is the proton gyrofrequency in radians; (2) He^+ band: $\omega_{lc} = 2.5\Omega_3$, $\omega_{uc} = 3.5\Omega_3$, $\omega_m = 3\Omega_3$, $\delta\omega = 0.5\Omega_3$, $\rho_1 = 0.7$, $\rho_2 = 0.2$, and $\rho_3 = 0.1$, where Ω_3 is the O^+ gyrofrequency in radians; (3) O^+ band: $\omega_{lc} = 0.85\Omega_3$, $\omega_{uc} = 0.95\Omega_3$, $\omega_m = 0.9\Omega_3$, $\delta\omega = 0.05\Omega_3$, $\rho_1 = 0.6$, $\rho_2 = 0.2$, and $\rho_3 = 0.2$. These wave frequency distributions are assumed to be L shell and latitudinally constant, and the waves have a maximum latitudinal coverage of 40° according to a recent survey of Cluster wave measurements by *Allen et al.* [2015]. In addition, in this study we focus

Table 1. EMIC Wave Normal Angle Distribution Parameters
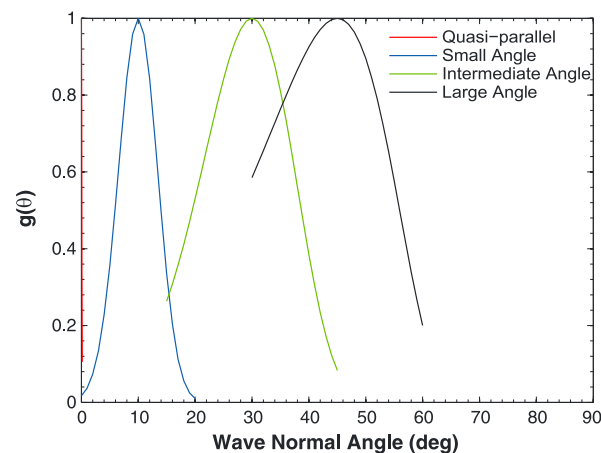
Latitudinally Constant Models			
Model	θ_m (°)	θ_w (°)	θ range (°)
Quasi-parallel	0	0.1	0–0.15
Small angle	10	10	0–20
Intermediate angle	30	15	15–45
Large angle	45	15	30–60
Latitudinally Varying Model			
$\|\lambda\|$ (°)	θ_m (°)	θ_w (°)	θ range (°)
0–5	0	0.1	0–0.15
5–15	10	10	0–20
15–30	30	15	15—45
30–40	45	15	30—60

on EMIC wave scattering of relativistic electrons at energies ≤10 MeV, while EMIC waves are more likely to resonate with higher energy electrons at latitudes above 40°. To investigate the sensitivity of EMIC wave scattering rates to wave normal angle distribution, we choose four Gaussian models (i.e., equation (3)) from the quasi-parallel distribution to the large angle distribution as listed in Table 1 and shown in Figure 1. As EMIC waves become more oblique, the majority of the wave power deviates from the field-aligned direction to the orientation of large angles with respect to the ambient magnetic field. On the basis of these four latitudinally constant models, we establish a more reliable model of EMIC wave normal angle distribution by including the latitudinal dependence, i.e., varying from the quasi-parallel propagation in the equatorial region to highly oblique direction at high latitudes as tabulated at the bottom of Table 1.

The Full Diffusion Code [*Ni et al.*, 2008, 2011; *Shprits and Ni*, 2009] is implemented to compute the quasi-linear bounce-averaged diffusion coefficients in the dipole field for various EMIC wave normal angle distributions. Especially, in a cold, multi-ion plasma, for obliquely propagating EMIC waves, resonant frequencies are obtained by the simultaneous solution of the Doppler-shifted resonance condition and the cold plasma dispersion relation, which turns out to satisfy a 14th-order polynomial equation, as described in the Appendix A. To deal with crossover and bi-ion frequencies, we follow the method described by *Albert* [2003] to treat them appropriately. Our calculations of EMIC wave-induced quasi-linear scattering coefficients include contributions from the $N = -5$ to $N = 5$ cyclotron harmonic resonances. The present study ignores the effect of the Landau resonance ($N = 0$), since the scattering rates tend to be at least several orders of magnitude smaller than those for the cyclotron resonances.

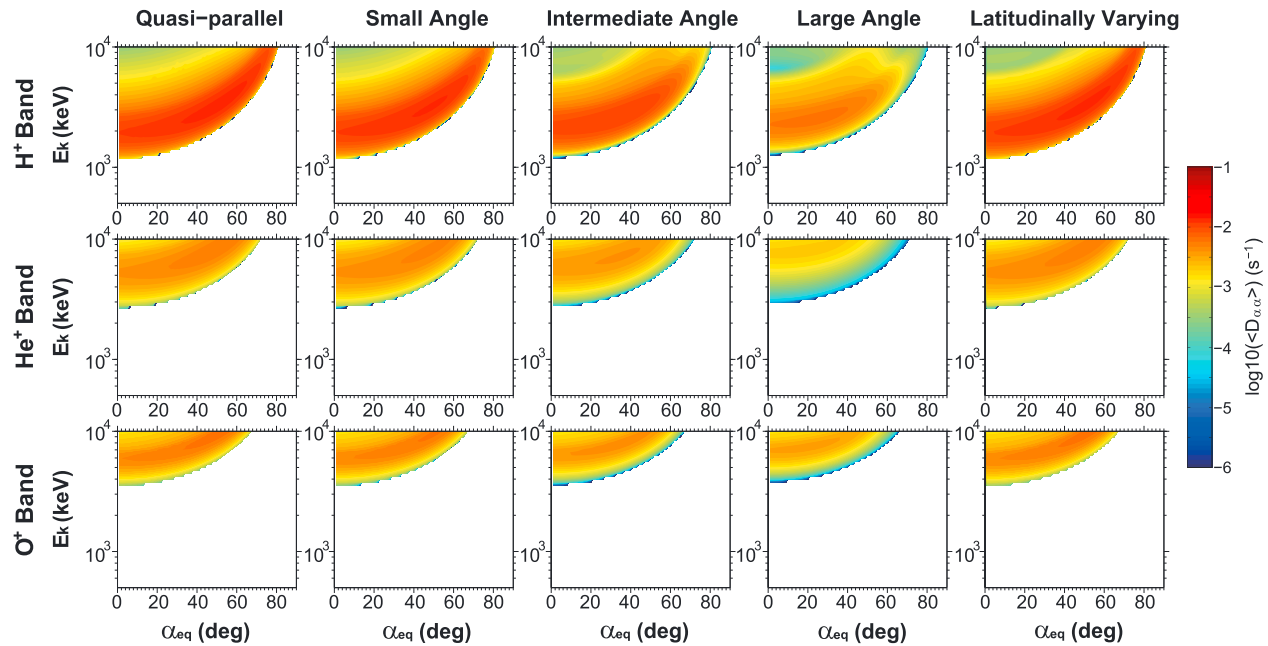## 3. EMIC Wave-Induced Scattering Rates and Loss Cone Filling Index

Figure 2 shows the 2-D plots of bounce-averaged pitch angle diffusion rates $<D_{\alpha\alpha}>$ as a function of equatorial pitch angle α_{eq} and electron kinetic energy E_k (0.5–10 MeV) at $L = 4$ for the three bands of EMIC waves (from top to bottom: H^+, He^+, and O^+) and the considered five wave normal angle distributions (from left to right). The electron density at $L = 4$ is 346 cm^{-3}, representative of a region in the plasmasphere. First, bounce-averaged pitch angle scattering rates strongly depend on the band of EMIC waves. While H^+-band waves can resonate with relativistic electrons just above 1 MeV, He^+-band and O^+-band waves only interact with ultrarelativistic electrons > ~3 MeV and > ~4 MeV, respectively. Given the same wave amplitude (i.e., 1 nT adopted as the nominal value), H^+-band wave scattering coefficients peak at 2–3 MeV with a rate on the order of 10^{-2} s^{-1}, but He^+-band and O^+-band wave scattering coefficients tend to maximize respectively at 5–6 MeV and 6–8 MeV at a rate of the order of 10^{-3} s^{-1}. Although H^+-band EMIC waves dominate the

Figure 1. Assumed four Gaussian distributions of EMIC wave power for various wave normal angle models, varying from the quasi-parallel propagation to highly oblique orientation.

Figure 2. 2-D plots of bounce-averaged pitch angle diffusion rates $<D_{\alpha\alpha}>$ as a function of equatorial pitch angle α_{eq} and electron kinetic energy E_k (0.5–10 MeV) at L = 4 for the three bands of EMIC waves (from top to bottom: H^+, He^+, and O^+) and the considered five wave normal angle distributions (from left to right).

scattering loss of $< {\sim}4$ MeV outer zone relativistic electrons, it is He^+-band and O^+-band waves that prevail over the pitch angle diffusion of ultrarelativistic electrons at much higher energies. As electron energy increases, scattering by EMIC waves extends to higher pitch angles, regardless of the EMIC wave band. Resonance with H^+-band waves takes place for the electron population with α_{eq} up to ${\sim}80°$, but resonances with He^+-band and O^+-band waves are well confined to $\alpha_{eq} < 66°$ for resonant energies below 10 MeV. Second, bounce-averaged pitch angle scattering rates rely on the EMIC wave normal angle distribution to a different extent with respect to the wave band. When the wave normal angle distribution varies from the quasi-parallel model to the large angle model (as shown in Figure 1), for all three bands of EMIC waves, pitch angle scattering rates decrease accordingly, demonstrating that obliquity of EMIC waves can reduce the efficiency of wave-induced relativistic electron scattering loss. In particular, as EMIC waves become moderately and highly oblique, $<D_{\alpha\alpha}>$ for H^+-band waves not only drops at most energies and pitch angles but also shows the double-peak profile at pitch angles of ${\sim}40°–70°$ for electrons $> {\sim}5$ MeV, owing to the contribution from higher order resonance harmonics. In contrast, contribution of higher-order resonances for relativistic electron resonant interactions with He^+-band and O^+-band waves is less significant, since the first-order resonance is dominant. However, the differences in scattering rates are easily discerned as well. Taking into account the latitudinal variation of wave normal angle, the latitudinally varying model provides a more realistic representation of the properties of EMIC wave propagation along the field line. Compared to the frequently adopted quasi-parallel model, use of this improved model produces the largest differences in scattering rates at pitch angles $< {\sim}40°$ for electrons $> {\sim}6$ MeV but almost no changes for the electron population with other energies or pitch angles. Since resonant electron energy increases with magnetic latitude, changes in EMIC wave normal angle distribution at higher latitudes are more likely to affect the efficiency of pitch angle scattering ultrarelativistic electrons at lower equatorial pitch angles.

Figure 3 shows the results of $<D_{\alpha\alpha}>$ similar to Figure 2, except for L = 6. The electron density at L = 6 is 49 cm^{-3}, representative of a region in the plasmaspheric plume. In principle, the major features of EMIC wave-driven electron scattering rates show dependences on the band of EMIC waves, the adopted wave normal angle model, electron kinetic energy, and equatorial pitch angle in a manner similar to those shown in Figure 2. However, resonant scattering of outer zone relativistic electrons at higher L shells has its particularity: (1) resonances can occur for relativistic electrons at lower energies, say, down to ${\sim}0.8$ MeV for H^+-band waves, to ${\sim}2$ MeV for He^+-band waves, and to ${\sim}3$ MeV for O^+-band waves,
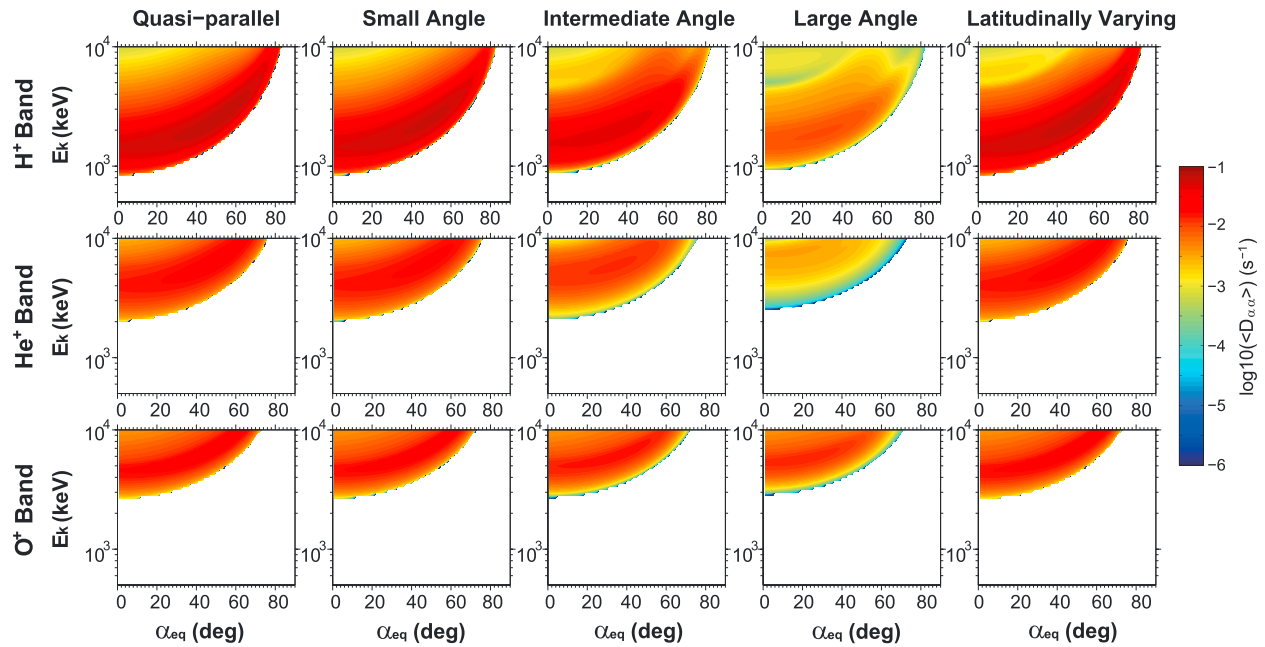
Figure 3. Same as in Figure 2 except for L = 6.

respectively, since the ratio of f_{pe}/f_{ce} increases with L shell and consequently lowers electron energies for gyroresonance; (2) resonant scattering rates are much stronger for all three EMIC wave bands and the considered wave normal angle models, since the EMIC wave amplitude is constantly adopted as 1 nT and consequently the ratio of B_W/B_0 increases as L shell increases. Overall, given the wave amplitude,
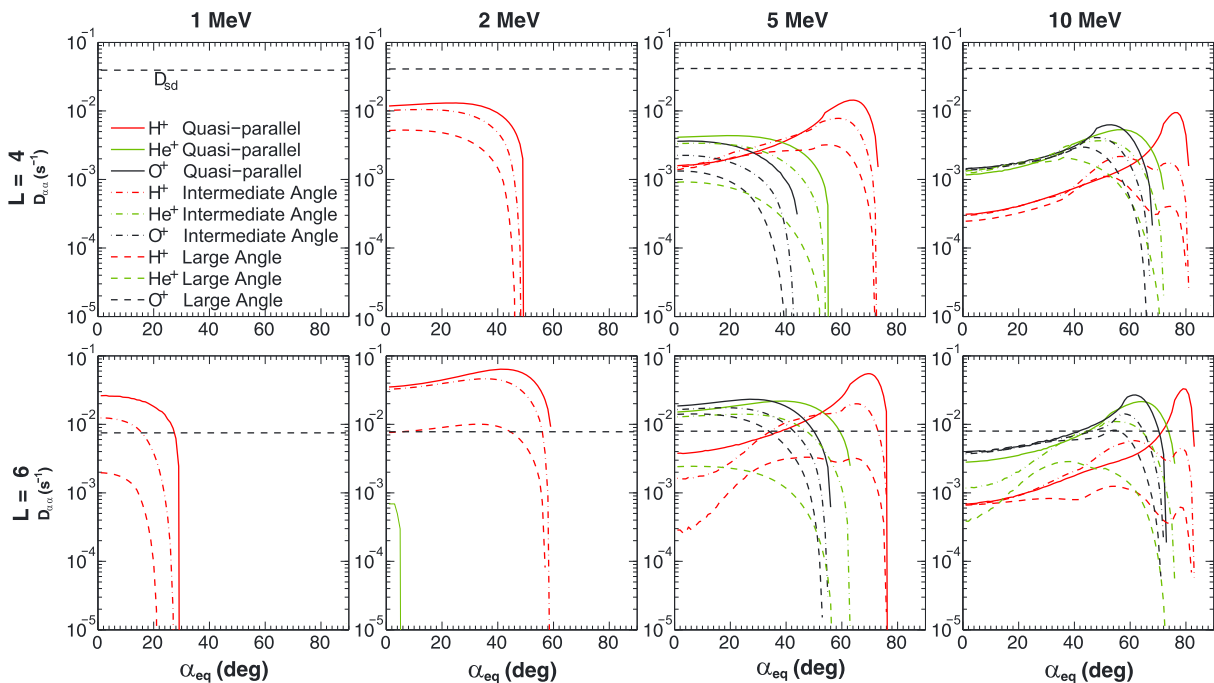

Figure 4. Line plots of bounce-averaged pitch angle scattering rates as a function of equatorial pitch angle for 1, 2, 5, and 10 MeV electrons at L = 4 and L = 6, corresponding to the three EMIC wave bands (H+, He+, and O+) and the three models of wave normal angle distribution (Quasi-parallel, Intermediate Angle, and Large Angle).

Figure 5. Profiles of loss cone filling index as a function of electron kinetic energy at L = 4 and L = 6, corresponding to the three EMIC wave bands (H^+, He^+, and O^+) and the five considered models of wave normal angle distribution.

EMIC waves at higher L shells tend to resonantly interact with a larger population of outer zone relativistic electrons and drive their pitch angle scattering loss more efficiently.
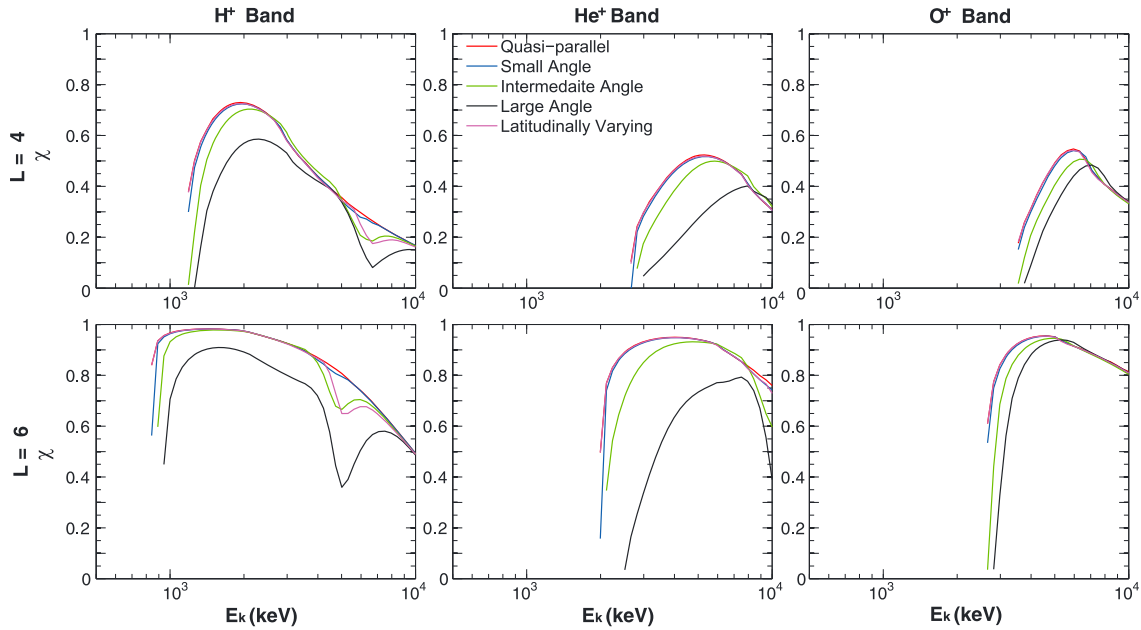
Figure 4 displays the line plots of bounce-averaged pitch angle scattering rates as a function of equatorial pitch angle for 1, 2, 5, and 10 MeV electrons at L = 4 and L = 6, corresponding to the three wave bands (H^+, He^+, and O^+) and the three models of wave normal angle distribution (Quasi-parallel, Intermediate Angle, and Large Angle). Overplotted is the horizontal line of the strong diffusion rate D_{SD}, which is determined by [*Summers and Thorne*, 2003]

$$D_{SD} \approx \frac{9.44}{L^4}\left(\frac{4L}{4L-3}\right)^{1/2}\frac{\left[\overline{E}(\overline{E}+2)\right]^{1/2}}{\overline{E}+1},$$

(5)

where L is the magnetic shell and $\overline{E} = E_k/(m_e c^2)$ is the electron kinetic energy in units of its rest energy with m_e as the electron mass, and c the speed of light. Strong diffusion is a concept that wave-induced pitch angle diffusion is strong enough to scatter particles across the loss cone for loss to the atmosphere within in times comparable with or less than the bounce period. The strong diffusion rate corresponds to a rate of scattering that drives the atmospheric loss of a particle at the equatorial loss cone with a quarter bounce period after traversing the equator. The effect of strong diffusion is to fill the loss cone and make the particle pitch angle distribution isotropic [*Kennel*, 1969; *Schulz*, 1974]. It is obvious that for EMIC waves with a nominal amplitude of 1 nT, while the wave scattering of relativistic electrons at L = 4 is well below the level of strong diffusion, the scattering at L = 6 becomes comparable or even exceeds the rate of strong diffusion. H^+-band EMIC waves can resonate with outer zone relativistic electrons > ~1 MeV, which can extend to higher pitch angles as electron energy increases. Obliquity of H^+-band wave produces considerable decrease in scattering rates at all pitch angles for 1–2 MeV electrons but preferentially confined at large pitch angles of $\alpha_{eq} >$ ~66° for 5–10 MeV electrons. In contrast, He^+-band and O^+-band EMIC waves cause more intense pitch angle scattering of >5 MeV electrons, the rates of which primarily drop at all pitch angles when the waves become more oblique.

When the strong diffusion rate (D_{SD}) and bounce-averaged pitch angle diffusion coefficients at the loss cone ($<D_{\alpha\alpha}>|_{LC}$) are available, the index of loss cone filling in association with the efficiency of EMIC wave-induced
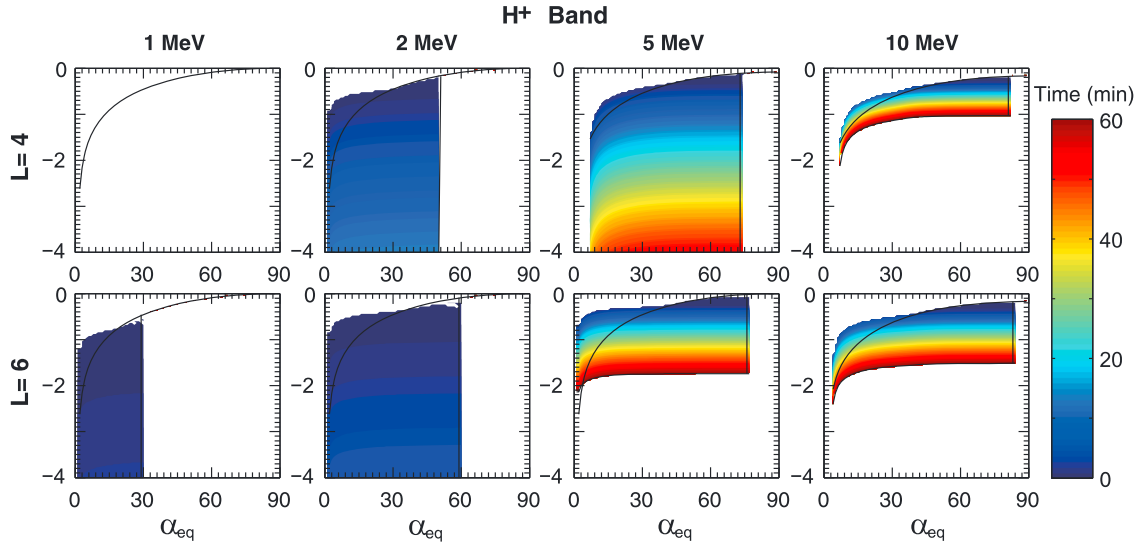
Figure 6. One-hour temporal variations of relativistic electron flux (normalized to the initial value at 90° pitch angle) and their pitch angle distributions at L = 4 and L = 6 for 1 MeV, 2 MeV, 5 MeV, and 10 MeV electrons under the impact of 1 nT H$^+$-band EMIC wave scattering with the latitudinally varying wave normal angle distribution. Color-coding denotes the time into the simulation, and the black curve indicates the initial electron flux.

scattering loss can be estimated using the following equation [e.g., *Kennel and Petschek*, 1966; *Ni et al.*, 2012, 2014a, 2014b],

$$\chi(E_k) = \frac{2\int_0^1 I_0\left[Z_0(E_k)\tau\right] \cdot \tau \cdot d\tau}{I_0\left[Z_0(E_k)\right]}, \tag{6}$$

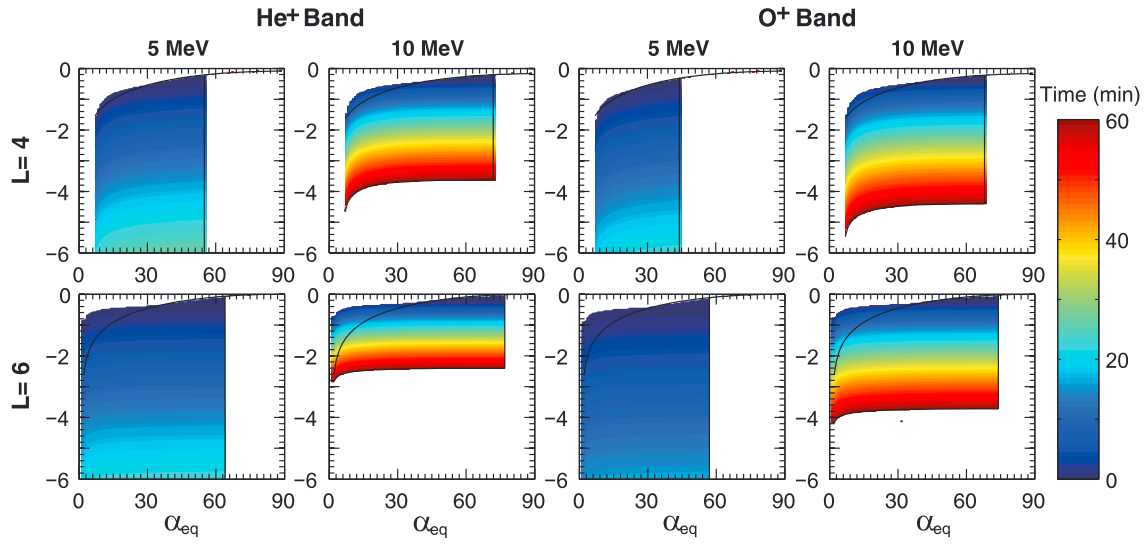where $Z_0 = [D_{SD}/<D_{\alpha\alpha}>|_{LC}]^{1/2}$ is an energy-dependent parameter defining the strength of the diffusion, and I_0 is the modified Bessel function of the first kind. As a parameter with the value between 0 and 1, the loss cone filling index describes a fully filled loss cone with a value of $> \sim 0.8$, a partially filled loss cone with a value of ~ 0.2–0.8, and an almost empty loss cone with a value $< \sim 0.2$. The results of loss cone filling index calculations are shown in Figure 5. Given the same wave amplitude, the strong diffusion limit is more likely to be reached at higher L shells. Specifically, at L = 4, only H$^+$-band waves can heavily or fully fill the loss cone for ~ 1–3 MeV electrons. At L=6, all three bands can produce the electron scattering loss in the regime of strong diffusion, i.e., at energies of ~ 1–5 MeV for H$^+$-band waves, of ~ 2–8 MeV for He$^+$-band waves, and of ~ 3–10 MeV for O$^+$-band waves. By comparison, pitch angle scattering by the latter two wave bands tends to trigger more intense loss cone filling for outer zone relativistic electrons than the former band. Use of the quasi-parallel and small angle models produces small differences in the loss cone filling index, but more oblique models of EMIC waves generally weaken the efficiency of filling the loss cone. In addition, when the latitudinal variation of EMIC wave normal angle distribution is considered, compared to the results for the commonly used quasi-parallel model, the consequence of loss cone filling is very similar for He$^+$-band and O$^+$-band waves, but becomes weaker for H$^+$-band waves interacting with ~ 6–8 MeV electrons at L = 4 and with ~ 4–6 MeV electrons at L = 6.

4. Pure Pitch Angle Diffusion Simulations and Electron Loss Time Scales

In order to investigate the temporal evolution of outer zone relativistic electron pitch angle distribution due to EMIC wave scattering, we perform the 1-D pure pitch angle diffusion simulations [e.g., *Meredith et al.*, 2006; *Thorne et al.*, 2013; *Ni et al.*, 2013, 2014a, 2014b] by numerically solving the equation

$$\frac{\partial f}{\partial t} = \frac{1}{T(\alpha_{eq})\sin(2\alpha_{eq})}\frac{\partial}{\partial\alpha_{eq}}\left[T(\alpha_{eq})\sin(2\alpha_{eq})\langle D_{\alpha\alpha}\rangle\frac{\partial f}{\partial\alpha_{eq}}\right], \tag{7}$$

Figure 7. Same as in Figure 6 except for resonant interactions of He$^+$-band and O$^+$-band EMIC waves with 5 MeV and 10 MeV electrons.

where f is the phase space density (PSD), t is the time, and the electron bounce period is approximated as $T(\alpha_{eq}) = 1.3802 - 0.3198\left[\sin(\alpha_{eq}) + \sqrt{\sin(\alpha_{eq})}\right]$ [*Lenchek et al.*, 1961]. The upper boundary condition for PSD in a_{eq} space is set as $\frac{\partial f}{\partial \alpha_{eq}}(\alpha_{eq} = 90°) = 0$, and the corresponding lower boundary condition is set as $\frac{\partial f}{\partial \alpha_{eq}}(\alpha_{eq} = 0°) = 0$ for the strong diffusion and as $f(\alpha_{eq} \leq \alpha_{LC}) = 0$ (where α_{LC} is the equatorial loss cone angle) for the weak diffusion. It is further assumed that the initial PSD follows a power law sinusoidal function of equatorial pitch angle, e.g., $\propto \sin^{1.5}\alpha_{eq}$ [e.g., *Ni et al.*, 2013].
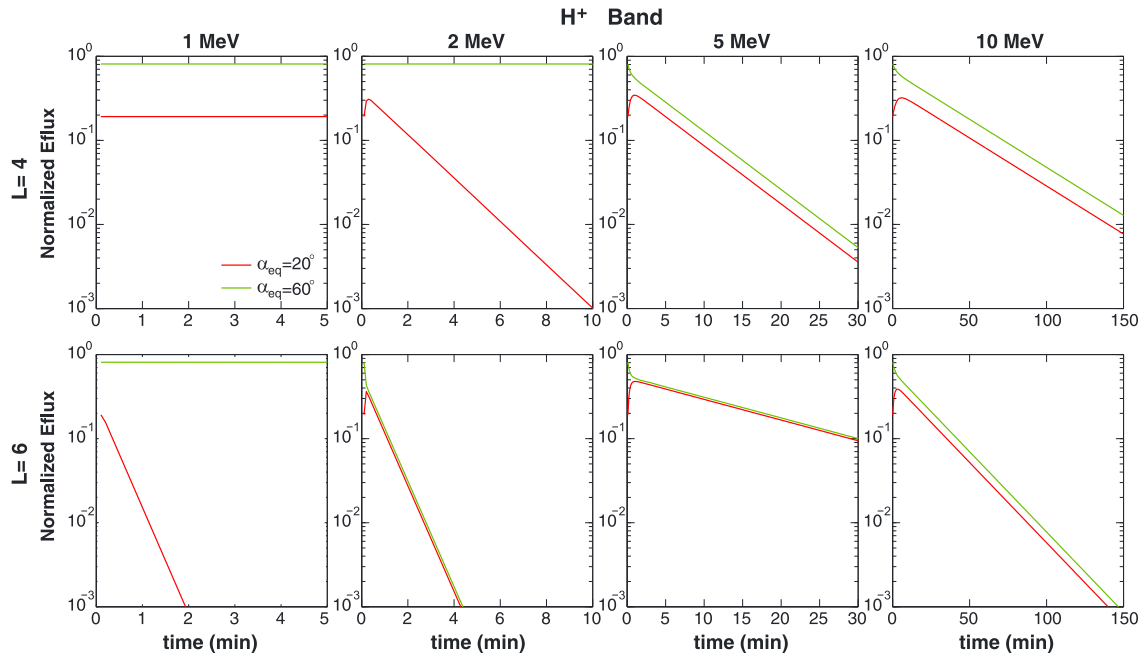

Figure 8. Corresponding to Figure 6, detailed pitch angle evolution of 1 MeV, 2 MeV, 5 MeV, and 10 MeV electron fluxes for indicated equatorial pitch angles, i.e., 20° and 60°, due to resonant scattering by 1 nT H$^+$-band EMIC waves with the latitudinally varying wave normal angle distribution.
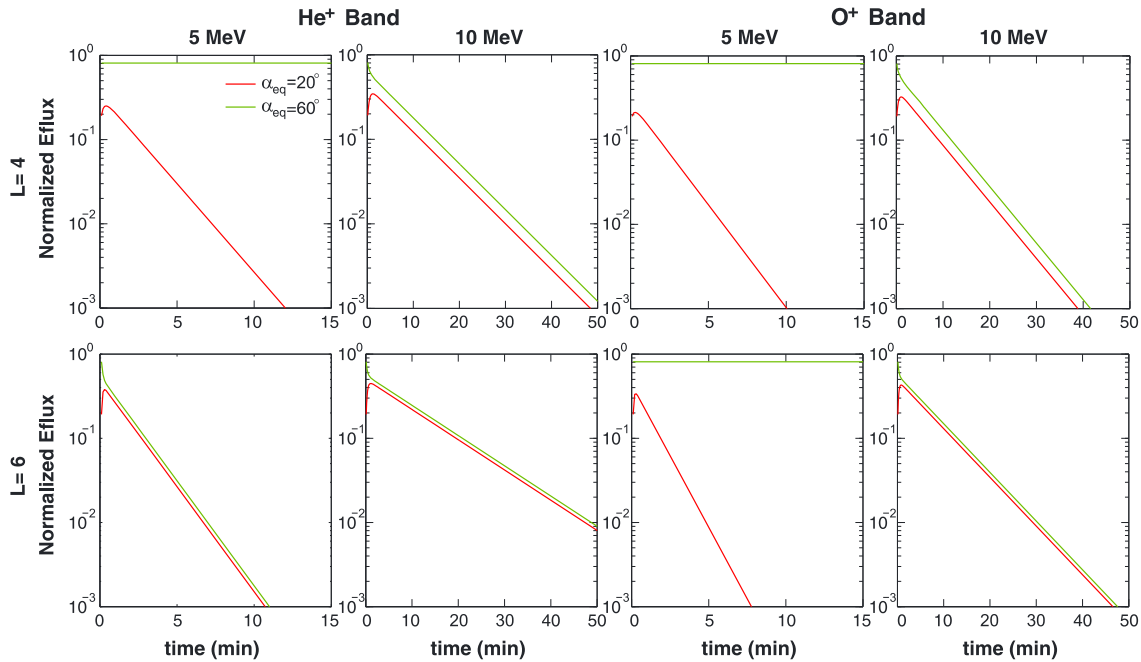
Figure 9. Corresponding to Figure 7, detailed pitch angle evolution of 5 MeV and 10 MeV electron fluxes for indicated equatorial pitch angles, i.e., 20° and 60°, due to resonant scattering by 1 nT He$^+$-band and O$^+$-band EMIC waves with the latitudinally varying wave normal angle distribution.

Figure 6 shows the 1 h temporal variations of relativistic electron flux (normalized to the initial value at 90° pitch angle) and their pitch angle distributions at $L = 4$ and $L = 6$ under the impact of 1 nT H$^+$-band EMIC wave scattering with the latitudinally varying wave normal angle distribution. Color-coding denotes the time into the simulation. Within a time span of 15 min, 1 MeV electrons at $L = 6$ and 2 MeV electrons at both $L = 4$ and $L = 6$ exhibit substantial flux decreases at lower pitch angles by at least 4 orders of magnitude, due to EMIC wave scattering. The loss cone is heavily filled quickly, while the electron fluxes remain unchanged at higher pitch angle since no scattering occurs with this population. Electrons of 5 and 10 MeV undergo relatively slower loss and decay and show an empty loss cone for the condition of weak diffusion. After reaching the equilibrium state in minutes or tens of minutes, these ultrarelativistic electron fluxes undergo a decay, extending to equatorial pitch angles much closer to 90°. Similar 2-D plots for He$^+$-band and O$^+$-band EMIC waves are shown in Figure 7 for 5 MeV and 10 MeV electrons. First, for both energies these two bands produce scattering loss and decay faster than H$^+$-band waves. Second, the loss cone is empty at $L = 4$ due to the weak diffusion but fully filled at $L = 6$ as a result of approaching the strong diffusion limit. Finally, compared to the results of $L = 4$ under the weak diffusion, approach of the strong diffusion at $L = 6$ accelerates the decay of 5 MeV electrons but slows down the decay of 10 MeV electrons after reaching the equilibrium state.

Corresponding to Figure 6, a detailed illustration of electron flux evolution for specific equatorial pitch angles is presented in Figure 8 for H$^+$-band EMIC waves. Two values of α_{eq}, 20° and 60°, are selected. Again, the modeled fluxes are normalized by the initial value at 90° pitch angle. There are a number of interesting features to address: (1) electron fluxes can keep intact with time, say, at $L = 4$ for 1 MeV electrons at the considered two pitch angles and for 2 MeV electrons at 60° pitch angle and at $L = 6$ for 1 MeV electrons at 60° pitch angle, since H$^+$-band EMIC waves cannot resonate with these electron populations. (2) While relativistic electron fluxes at energies of 2, 5, and 10 MeV decrease with time for 60° pitch angle (except for 2 MeV electrons at $L = 4$), they exhibit an initial increase and a subsequent decrease for 20° pitch angle, which indicates the underlying transport of the electron population from high pitch angles to lower pitch angles due to EMIC wave-induced scattering and its dependence on equatorial pitch angle. (3) In principle, the time required to reach the flux equilibrium state is very short, e.g., <1 min for 2 MeV electron, <2 min for 5 MeV electrons, and <5 min for 10 MeV electrons. This relaxation time also decreases with increasing L shell and equatorial pitch angle but increases with electron energy. (4) After reaching the equilibrium relativistic electron fluxes decay exponentially with time,
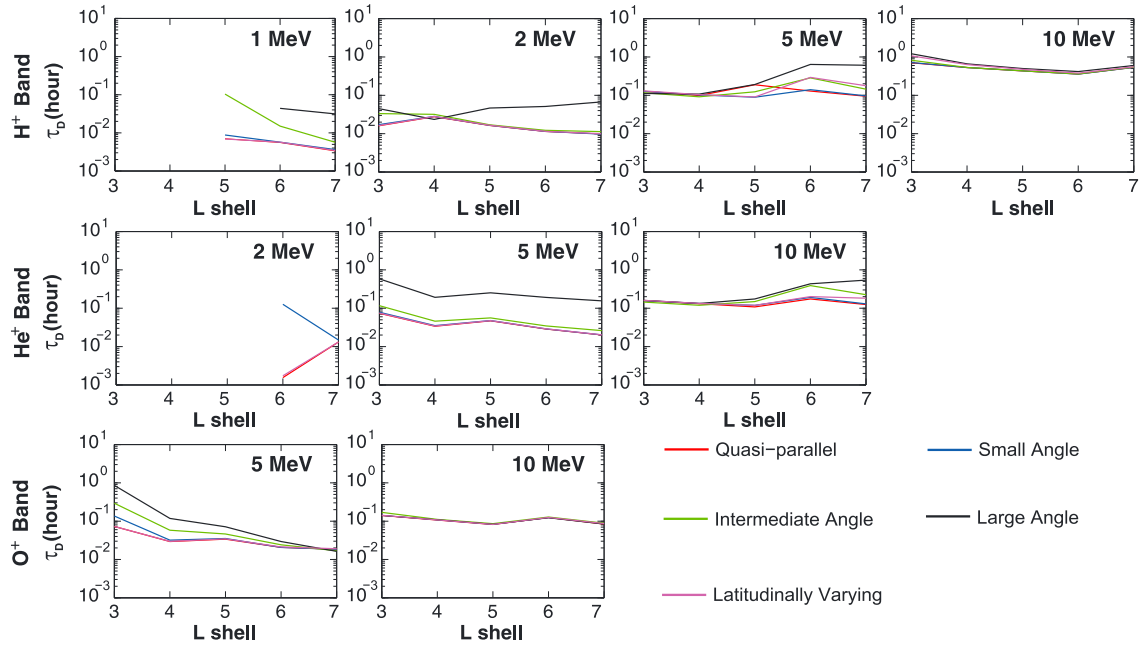
Figure 10. Time scales (τ_D) associated with the flux exponential decay following the equilibrium state as a function of L shell for the indicated electron energies corresponding to the three EMIC wave bands and the five considered models of wave normal angle distribution.

independent of equatorial pitch angle. Compared to the results at L = 4, relativistic (0.5–1.5 MeV) electron fluxes decay at L = 6 are faster for 2 MeV and 10 MeV electrons primarily due to stronger rates of wave scattering, but slower for 5 MeV partially due to the sharp flux gradient at small pitch angles associated with the empty loss cone (as shown in Figure 6). Figure 9 shows the electron flux evolution for specific equatorial pitch angles for He$^+$-band and O$^+$-band EMIC waves. We can capture the features of ultrarelativistic electron flux evolution similar to those shown in Figure 8, including the dependence on L shell, electron energy, and equatorial pitch angle and the two-stage process of relaxation to the equilibrium and subsequent exponential decay. In addition, at the same amplitude, He$^+$-band and O$^+$-band EMIC waves tend to drive similar scattering effects, which, however, cause more rapid relaxation toward equilibrium and more efficient exponential decay of 5–10 MeV electrons than H$^+$-band waves.

To quantify the electron loss time scale (τ_D) associated with the exponential decay as a whole following the equilibrium state, we compute it as follows:

$$\tau_D = -\frac{t_{n+1} - t_n}{\ln\left[j_{n+1}\left(\alpha_{\mathrm{eq}}\right)\right] - \ln\left[j_n\left(\alpha_{\mathrm{eq}}\right)\right]}, \tag{8}$$

where the subscript "n" denotes the index of the simulation time step and is selected much larger than the index when the equilibrium state is reached. The results are shown in Figure 10 as a function of L shell, corresponding to the indicated relativistic electron energies for the three EMIC wave bands and the color-coded five wave normal angle distributions. In general, EMIC waves, at a nominal representative amplitude of 1 nT, produce intense scattering losses of outer radiation belt relativistic electron on time scales that range from <1 min to ~1 h. Variations of wave normal angle distribution can introduce distinct differences in EMIC wave-induced electron loss time scales for 1, 2, and 5 MeV electrons but much smaller (or negligible) differences for 10 MeV electrons. Electron loss time scales primarily increases with kinetic energy, but decreases with L shell for the adopted latitudinally varying wave normal angle model. By comparison, H$^+$-band waves are most efficient in producing the pitch angle scattering loss of 1 MeV electrons at L ≥ 5 and of 2 MeV electrons at L < 6, He$^+$-band waves of 2 MeV electrons at L ≥ 6, and O$^+$-band waves of 5 MeV and 10 MeV electrons in the entire region of the outer zone.

5. Discussion

While the intensity of EMIC waves varies with the level of geomagnetic activity and the spatial location [e.g., *Usanova et al.*, 2012; *Min et al.*, 2012; *Meredith et al.*, 2014], in the present study, for simplicity, we have adopted a nominal intermediate amplitude of 1 nT for all three bands of EMIC waves. This value is consistent with the AMPTE survey results that the average power spectral density typically lies between 1 and 10 nT^2/Hz [*Anderson et al.*, 1992a, 1992b] with a peak-to-peak wave amplitude of about 1.6 nT and between the CRRES survey results [*Meredith et al.*, 2014] and the model results used by *Kersten et al.* [2014]. Despite the differences, as long as the wave activity is not strong enough ($< \sim 2$ nT) to trigger any nonlinear effect [e.g., *Albert and Bortnik*, 2009], quasi-linear bounce-averaged diffusion coefficients for different EMIC wave power can be easily obtained by scaling the results shown here by the square of wave amplitude. Correspondingly, the resultant electron loss time scales are linearly proportional to the inverse of the square of wave amplitude. In addition, we have adopted different ratios of ion composition for the three EMIC wave bands. There are two major reasons to justify this treatment. First and most importantly, excitation and amplification of different EMIC wave bands require different conditions including source ion population, geomagnetic activity, spatial location, and even solar cycle. For instance, increase in the composition of He$^+$ and O$^+$ can result in preferential generation and intensification of He$^+$-band and O$^+$-band EMIC waves, respectively. While it is possible that the three bands can be observed simultaneously, the more general case is that each band has its specific preferential profile of ion composition for growth, which can also explain why O$^+$-band EMIC waves are observed with the occurrence rate much smaller than the other two bands. Second, we have followed a number of previous studies [e.g., *Summers and Thorne*, 2003; *Albert*, 2003 JGR; *Summers et al.*, 2007] to choose the three different but representative ion compositions for computing the scattering rates by the three EMIC wave band, which we think is reasonable for this effort of numerical computation and theoretical analysis.

Although bounce averaging is applied to EMIC wave-induced scattering coefficients, the drift-averaging that takes into account the MLT coverage of EMIC waves is not considered in the present study. The reason is twofold: (1) bounce-averaged diffusion coefficients can provide the rates of localized scattering loss along any specific geomagnetic field line, and therefore, the efficiency of loss cone filling can be reasonably quantified; (2) the drift-averaging procedure can be simply done by multiplying the bounce-averaged diffusion coefficients by the percentage of EMIC wave occurrence over all MLTs once available. For instance, *Summers et al.* [2007] adopted 1% drift averaging for the considered three EMIC wave bands constantly; *Li et al.* [2007] adopted 5% drift averaging during the storm main phase and 1% drift averaging during the storm recovery phase for the considered He$^+$-band EMIC waves. Recently, *Kersten et al.* [2014] adopted 25% drift averaging for the considered H$^+$-band and He$^+$-band EMIC waves, and *Ma et al.* [2015] adopted 2% drift averaging for the considered He$^+$-band EMIC waves. There is also recent evidence that the EMIC wavefield can extend over much larger MLT regions than previously believed, ~ 12 h in local time or more [*Engebretson et al.*, 2015], thus creating the possibility that the entire EMIC-driven scattering process described above could indeed take place over ~ 1 min time scales, within a single drift orbit of the energetic electron population. Application of drift averaging takes account of the fractional encounter with waves during each trajectory of electron drift orbits, thereby decreasing the bounce-averaged scattering rates and increasing the electron loss time scales.

While the parallel or quasi-parallel propagation assumption has been widely used to evaluate the rates of EMIC wave scattering in the past, the present study has comprehensively investigated its sensitivity to wave normal angle distribution by adopting four latitudinally constant models that cover from the quasi-parallel propagation to the highly oblique orientation and one latitudinally varying model. The results indicate that, while intermediate or large angle models can introduce considerable decreases of the outer zone scattering rates, a more realistic latitudinally dependent model produces the bounce-averaged diffusion coefficients similar to that for the quasi-parallel model except for $> \sim 5$ MeV electrons interacting with H$^+$-band EMIC waves. In other words, parallel or quasi-parallel wave normal angle distribution tends to behave as a good approximation, especially for He$^+$-band and O$^+$-band EMIC waves.

Our pure pitch angle diffusion simulations demonstrate that for EMIC wave-induced scattering loss, when the electron pitch angle distribution reaches an equilibrium shape, the decay of electron flux follows an exponential drop that can be described by a single lifetime parameter and is independent of electron pitch

angle, except for the electron population at high pitch angles that is out of resonance with EMIC waves and remains intact in the outer radiation belt. As a consequence, EMIC wave scattering has the potential to deepen the anisotropic distribution of relativistic electrons by leaving their pitch angle profiles more likely as a "top-hat" shape. To perform the pitch angle diffusion simulations, we have adopted the sinusoidal function as the initial electron pitch angle distribution, and either empty loss cone or zero PSD gradient (depending on the extent of loss cone filling) as the lower boundary condition. We note that electron loss rate depends not only on pitch angle scattering rates near the loss cone but also the PSD gradient with respect to pitch angle. Near the strong diffusion limit, resonant scattering by EMIC waves tends to cause a prompt transition to the equilibrium state, and the ensuing exponential decay behavior is predominantly controlled by the scattering rates near the equatorial loss cone. In the regime of weak diffusion, while longer time is required to reach the equilibrium, empty loss cone (i.e., large gradient at the outer edge of the loss cone), together with the weak scattering by EMIC waves, can drive efficient decay even faster than the strong diffusion case.

Compared to the recent study of *Kersten et al.* [2014] concerning radiation belt electron losses caused by EMIC waves, the results obtained in the present study show both similarities and differences. The major similarities include that (1) EMIC wave scattering is highly energy selective, only occurring for $> \sim 1$ MeV electrons, depending on the L shell and wave band; (2) while EMIC waves can cause efficient scattering loss of $> \sim 1$ MeV relativistic electrons near the loss cone, the electron population at large pitch angles cannot undergo resonant interactions with EMIC waves, and therefore the latter seems unlikely to fully explain the storm time outer zone flux dropouts [e.g., *Reeves et al.*, 2003; *Turner et al.*, 2014a, 2014b]. Complementary to the above points, our investigation comprehensively assesses the effectiveness of EMIC waves in affecting the outer radiation belt electron dynamics by computing EMIC wave-driven relativistic electron scattering rates and loss cone filling index and evaluating the resultant electron pitch angle evolution and loss time scales in the broad spatial coverage of L = 3–7, corresponding to different EMIC wave bands and different wave normal angle models. There turn out to be a number of important findings: (1) although quasi-parallel propagation can be a good assumption for studying the scattering effect of He^+-band and O^+-band EMIC waves, the wave obliquity at higher latitudes can become important for scattering $> \sim 5$ MeV electrons by H^+-band EMIC waves; (2) while O+−band EMIC waves are not observed so frequently as the other two bands, they, once present, can cause considerable pitch angle scattering of ≥ 5 MeV electrons at rates comparable to those caused by He^+-band EMIC waves. (3) Given the same wave amplitude, strong diffusion by EMIC waves are more likely to occur for lower energy relativistic electrons at high L shells. A typical amplitude of 1 nT is strong enough to induce the rapid depletion of outer belt relativistic electrons on a time scale of seconds to hours.

Our calculations are based upon the cold plasma theory, which, however, can break down when the hot proton and/or electron density becomes comparable to or even exceed the cold plasma density, which can be the case during the intensification of substorm injections [e.g., *Chen et al.*, 2011; *Silin et al.*, 2011]. Inclusion of thermal plasma effects can introduce large differences in the determination of resonant frequencies and resonant scattering rates as well. Using an improved dispersion relation for parallel propagating EMIC waves in warm plasmas, *Chen et al.* [2013] found significant differences of local pitch angle scattering rates of MeV electrons caused by He+−band EMIC waves in multiple ion plasmas, compared to the results for the cold plasma dispersion relation. Evaluations of bounce-averaged diffusion coefficients by multiband EMIC waves in the realistic hot plasma environment are important to acquire improved understanding of the role of EMIC waves in the processes of outer zone relativistic electron loss, especially during geomagnetically disturbed periods, which requires careful investigation in future studies. In addition, when EMIC wave amplitudes are large, nonlinear resonant interactions can occur, leading to advection toward large pitch angles [*Albert and Bortnik*, 2009] and flattening of pitch angle distribution caused by nonlinear phase trapping and bunching [*Liu et al.*, 2012], both of which will reduce the precipitation losses of relativistic electrons. The nonlinear interaction between highly intense EMIC waves and radiation belt relativistic electrons is another subject that is left as a future study.

6. Conclusions

In the present study we have performed a comprehensive analysis of EMIC wave-induced resonant scattering of outer zone relativistic electrons and resultant electron loss time scales, corresponding to

different EMIC wave bands, different L shells, and different wave normal angle models. The main conclusions are summarized below:

1. While H^+-band EMIC waves dominate the scattering loss of ~1–4 MeV outer zone relativistic electrons, it is He^+-band and O^+-band waves that prevail over the pitch angle diffusion of ultrarelativistic electrons at higher energies. As electron energy increases, scattering by EMIC waves extends to higher pitch angles, regardless of the EMIC wave band. Resonance with H^+-band waves occurs for the electron population with α_{eq} up to ~80°, but resonances with He^+-band and O^+-band waves are confined to $\alpha_{eq} < 66°$ for electron energies <10 MeV. For a given wave amplitude, EMIC waves at higher L shells tend to resonantly interact with a larger population of outer zone relativistic electrons and drive their pitch angle scattering more efficiently.

2. Obliquity of EMIC waves can reduce the efficiency of wave-induced relativistic electron pitch angle scattering. As the waves become oblique, the contribution from higher- order resonance harmonics is nonnegligible for H^+-band emissions. Compared to the frequently adopted quasi-parallel model, use of the latitudinally varying wave normal angle model produces the largest differences in scattering rates at pitch angles < ~40° for electrons > ~5 MeV but small changes for the other electron population. Correspondingly, the consequence of loss cone filling is very similar for He^+-band and O^+-band waves, but becomes weaker for H^+-band waves interacting with ~ 6–8 MeV electrons at L = 4 and with ~4–6 MeV electrons at L = 6.

3. Under the impact of EMIC wave scattering, outer belt relativistic electron fluxes can reach the equilibrium state in minutes or tens of minutes, and then decay as a whole extending to higher equatorial pitch angles. The loss cone can be either empty as a result of the weak diffusion or heavily/fully filled due to the approach of the strong diffusion limit. In addition, the trapped electron population at high pitch angles close to 90° stays intact because of no resonant scattering. Therefore, EMIC wave scattering has the potential to deepen the anisotropic distribution of outer zone relativistic electrons by leaving their pitch angle profiles in space more likely as a top-hat shape.

4. At a representative nominal amplitude of 1 nT, EMIC produces intense decay losses of outer radiation belt relativistic electron on time scales that range from <1 min to ~1 h. Electron loss time scales primarily increases with kinetic energy, but decreases with L shell for the adopted latitudinally varying wave normal angle model. Overall, H^+-band and He^+-band EMIC waves are most efficient in producing the pitch angle scattering loss of relativistic electrons at ~1–2 MeV. In contrast, the presence of O^+-band EMIC waves, while at a smaller occurrence rate, can dominate the scattering loss of 5–10 MeV electrons in the entire region of the outer zone, which should be taken into account for future modeling of the outer zone relativistic electron dynamics. In addition, resonant interactions between EMIC waves and radiation belt relativistic electrons cannot scatter the population at large pitch angles. Therefore, scattering by EMIC waves alone is unlikely to fully explain radiation belt electron dropout events in which other loss mechanisms such as scattering by chorus and hiss can play an important role.

Appendix A: Calculation of EMIC Wave Resonant Frequencies in Cold Multi-ion Plasmas

The general dispersion relation for electromagnetic waves in a cold, magnetized multi-ion (H^+, He^+, O^+) plasma is given by

$$D(\omega, k, x) = (Sx^2 + P)\mu^4 - (RLx^2 + PS(2 + x^2))\mu^2 + PRL(1 + x^2) = 0, \qquad (A1)$$

where R, L, S, and P are the Stix parameters [*Stix*, 1962] and $\mu = |k|c/\omega$ is the wave refractive index. The resonant frequencies are obtained by the simultaneous solution of the resonance condition and the dispersion relation, which satisfies a 14th-order polynomial equation for resonant interactions between oblique EMIC waves and charged particles,

$$A_0\omega^{14} + A_1\omega^{13} + A_2\omega^{12} + A_3\omega^{11} + A_4\omega^{10} + A_5\omega^9 + A_6\omega^8 + A_7\omega^7 + A_8\omega^6$$
$$+ A_9\omega^5 + A_{10}\omega^4 + A_{11}\omega^3 + A_{12}\omega^2 + A_{13}\omega + A_{14} = 0 \qquad (A2)$$

where

$A_0 = (x^2 + 1)(N_2{}^2 - 1)^2,$

$A_1 = -4(x^2 + 1)N_1 N_2{}^2(N_2{}^2 - 1),$

$A_2 = (6(x^2 + 1)N_1{}^2 + B_1)N_2{}^4 - (2(x^2 + 1)N_1{}^2 + D_1)N_2{}^2 + (x^2 + 1)C_1,$

$A_3 = -4((x^2 + 1)N_1{}^3 + B_1 N_1)N_2{}^4 + 2N_1 D_1 N_2{}^2,$

$A_4 = ((x^2 + 1)N_1{}^4 + 6B_1 N_1{}^2 + B_2)N_2{}^4 - (D_1 N_1{}^2 + D_2)N_2{}^2 + (x^2 + 1)C_2,$

$A_5 = -4(B_1 N_1{}^3 + B_2 N_1)N_2{}^4 + 2N_1 D_2 N_2{}^2,$

$A_6 = (B_1 N_1{}^4 + 6B_2 N_1{}^2 + B_3)N_2{}^4 - (D_2 N_1{}^2 + D_3)N_2{}^2 + (x^2 + 1)C_3,$

$A_7 = -4(B_2 N_1{}^3 + B_3 N_1)N_2{}^4 + 2N_1 D_3 N_2{}^2,$

$A_8 = (B_2 N_1{}^4 + 6B_3 N_1{}^2 + B_4)N_2{}^4 - (D_3 N_1{}^2 + D_4)N_2{}^2 + (x^2 + 1)C_4,$

$A_9 = -4(B_3 N_1{}^3 + B_4 N_1)N_2{}^4 + 2N_1 D_4 N_2{}^2,$

$A_{10} = (B_3 N_1{}^4 + 6B_4 N_1{}^2 + B_5)N_2{}^4 - (D_4 N_1{}^2 + D_5)N_2{}^2 + (x^2 + 1)C_5,$

$A_{11} = -4(B_4 N_1{}^3 + B_5 N_1)N_2{}^4 + 2N_1 D_5 N_2{}^2,$

$A_{12} = (B_4 N_1{}^4 + 6B_5 N_1{}^2)N_2{}^4 - D_5 N_1{}^2 N_2{}^2 + (x^2 + 1)C_6,$

$A_{13} = -4B_5 N_1{}^3 N_2{}^4,$

$A_{14} = B_5 N_1{}^4 N_2{}^4,$

$B_1 = -\Omega_e{}^2 - \Omega_1{}^2 - \Omega_2{}^2 - \Omega_3{}^2 - \eta_{10} - \eta_1 x^2,$

$B_2 = \Omega_1{}^2(\Omega_2{}^2 + \Omega_3{}^2 + \Omega_e{}^2) + \Omega_2{}^2(\Omega_3{}^2 + \Omega_e{}^2) + \Omega_3{}^2 \Omega_e{}^2 + \eta_{10}(\Omega_1{}^2 + \Omega_2{}^2 + \Omega_3{}^2 + \Omega_e{}^2) + \eta_2 x^2$

$B_3 = -(\Omega_1{}^2(\Omega_2{}^2 \Omega_3{}^2 + \Omega_2{}^2 \Omega_e{}^2 + \Omega_3{}^2 \Omega_e{}^2) + \Omega_2{}^2 \Omega_3{}^2 \Omega_e{}^2$
$\qquad + \eta_{10}(\Omega_1{}^2 \Omega_2{}^2 + \Omega_1{}^2 \Omega_3{}^2 + \Omega_1{}^2 \Omega_e{}^2 + \Omega_2{}^2 \Omega_3{}^2 + \Omega_2{}^2 \Omega_e{}^2 + \Omega_3{}^2 \Omega_e{}^2)) - \eta_3 x^2$

$B_4 = \Omega_1{}^2 \Omega_2{}^2 \Omega_3{}^2 \Omega_e{}^2 + \eta_{10}(\Omega_1{}^2 \Omega_2{}^2 \Omega_3{}^2 + \Omega_1{}^2 \Omega_2{}^2 \Omega_e{}^2 + \Omega_1{}^2 \Omega_3{}^2 \Omega_e{}^2 + \Omega_2{}^2 \Omega_3{}^2 \Omega_e{}^2) + \eta_4 x^2$

$B_5 = -\eta_{10} \Omega_e{}^2 \Omega_1{}^2 \Omega_2{}^2 \Omega_3{}^2,$

$C_1 = -\eta_5{}^2 + 2\eta_6 - \eta_{10},$

$C_2 = \eta_{10} \eta_5{}^2 - 2\eta_7 \eta_5 + \eta_6{}^2 - 2\eta_{10}\eta_6 + 2\eta_8,$

$C_3 = -\eta_{10}\eta_6{}^2 + 2\eta_8\eta_6 - \eta_7{}^2 + 2\eta_5\eta_{10}\eta_7 + 2\eta_5\eta_9 - 2\eta_8\eta_{10},$

$C_4 = \eta_{10}\eta_7{}^2 + 2\eta_9\eta_7 + \eta_8{}^2 - 2\eta_6\eta_{10}\eta_8 - 2\eta_5\eta_9\eta_{10},$

$C_5 = -\eta_{10}\eta_8{}^2 - \eta_9{}^2 - 2\eta_7\eta_{10}\eta_9,$

$C_6 = \eta_9{}^2 \eta_{10},$

$D_1 = 2\eta_6 x^2 - 2\eta_{10} - \eta_1 x^2 - 2\eta_1 - \eta_{10}x^2 - \eta_5{}^2 x^2,$

$D_2 = 2\eta_2 + \eta_2 x^2 + 2\eta_8 x^2 + \eta_6{}^2 x^2 + 2\eta_1\eta_{10} + \eta_1\eta_{10}x^2 - 2\eta_5\eta_7 x^2,$

$D_3 = 2\eta_5\eta_9 x^2 - \eta_3 x^2 - \eta_7{}^2 x^2 - 2\eta_2\eta_{10} - \eta_2\eta_{10}x^2 - 2\eta_3 + 2\eta_6\eta_8 x^2,$

$D_4 = 2\eta_4 + \eta_4 x^2 + \eta_8{}^2 x^2 + 2\eta_3\eta_{10} + \eta_3\eta_{10}x^2 + 2\eta_7\eta_9 x^2,$

$D_5 = -\eta_9{}^2 x^2 - \eta_4\eta_{10}x^2 - 2\eta_4\eta_{10},$

$\eta_1 = \Omega_e{}^2 + \Omega_1{}^2 + \Omega_2{}^2 + \Omega_3{}^2 + \omega_{p1}{}^2 + \omega_{p2}{}^2 + \omega_{p3}{}^2 + \omega_{pe}{}^2,$

$\eta_2 = \Omega_e{}^2(\Omega_1{}^2 + \Omega_2{}^2 + \Omega_3{}^2 + \omega_{p1}{}^2 + \omega_{p2}{}^2 + \omega_{p3}{}^2 + \omega_{pe}{}^2) + \Omega_1{}^2(\Omega_2{}^2 + \Omega_3{}^2 + \omega_{p2}{}^2 + \omega_{p3}{}^2 + \omega_{pe}{}^2)$
$\qquad + \Omega_2{}^2(\Omega_3{}^2 + \omega_{p1}{}^2 + \omega_{p3}{}^2 + \omega_{pe}{}^2) + \Omega_3{}^2(\omega_{p1}{}^2 + \omega_{p2}{}^2 + \omega_{pe}{}^2),$

$\eta_3 = \Omega_e{}^2(\Omega_1{}^2 \Omega_2{}^2 + \Omega_1{}^2 \Omega_3{}^2 + \Omega_2{}^2 \Omega_3{}^2 + \Omega_1{}^2 \omega_{p2}{}^2 + \Omega_1{}^2 \omega_{p3}{}^2 + \Omega_2{}^2 \omega_{p1}{}^2 + \Omega_2{}^2 \omega_{p3}{}^2 + \Omega_3{}^2 \omega_{p1}{}^2 + \Omega_3{}^2 \omega_{p2}{}^2)$
$\qquad + \Omega_1{}^2(\Omega_2{}^2 \Omega_3{}^2 + \Omega_2{}^2 \omega_{p3}{}^2 + \Omega_2{}^2 \omega_{pe}{}^2 + \Omega_3{}^2 \omega_{p2}{}^2 + \Omega_3{}^2 \omega_{pe}{}^2) + \Omega_2{}^2(\Omega_3{}^2 \omega_{p1}{}^2 + \Omega_3{}^2 \omega_{pe}{}^2),$

$\eta_4 = \Omega_e{}^2 \Omega_1{}^2 \Omega_2{}^2 \Omega_3{}^2 + \Omega_e{}^2 \Omega_1{}^2 \Omega_2{}^2 \omega_{p3}{}^2 + \Omega_e{}^2 \Omega_1{}^2 \Omega_3{}^2 \omega_{p2}{}^2 + \Omega_e{}^2 \Omega_2{}^2 \Omega_3{}^2 \omega_{p1}{}^2 + \Omega_1{}^2 \Omega_2{}^2 \Omega_3{}^2 \omega_{pe}{}^2,$

$\eta_5 = \Omega_e + \Omega_1 + \Omega_2 + \Omega_3,$

$\eta_6 = -\omega_{p1}{}^2 - \omega_{p2}{}^2 - \omega_{p3}{}^2 - \omega_{pe}{}^2 + \Omega_1(\Omega_2 + \Omega_3 + \Omega_e) + \Omega_2(\Omega_3 + \Omega_e) + \Omega_3 \Omega_e,$

$\eta_7 = \Omega_1 \Omega_2 \Omega_3 + \Omega_1 \Omega_2 \Omega_e + \Omega_1 \Omega_3 \Omega_e + \Omega_2 \Omega_3 \Omega_e - \omega_{p1}{}^2(\Omega_2 + \Omega_3 + \Omega_e) - \omega_{p2}{}^2(\Omega_3 + \Omega_e + \Omega_1)$
$\qquad - \omega_{p3}{}^2(\Omega_1 + \Omega_2 + \Omega_e) - \omega_{pe}{}^2(\Omega_2 + \Omega_3 + \Omega_1),$

$\eta_8 = \Omega_1 \Omega_2 \Omega_3 \Omega_e - \omega_{p1}{}^2(\Omega_2 \Omega_3 + \Omega_2 \Omega_e + \Omega_3 \Omega_e) - \omega_{p2}{}^2(\Omega_1 \Omega_3 + \Omega_1 \Omega_e + \Omega_3 \Omega_e)$
$\qquad - \omega_{p3}{}^2(\Omega_1 \Omega_e + \Omega_2 \Omega_e + \Omega_1 \Omega_2) - \omega_{pe}{}^2(\Omega_1 \Omega_2 + \Omega_1 \Omega_3 + \Omega_2 \Omega_3),$

$\eta_9 = \Omega_e \Omega_2 \Omega_3 \omega_{p1}{}^2 + \Omega_1 \Omega_e \Omega_3 \omega_{p2}{}^2 + \Omega_1 \Omega_2 \Omega_e \omega_{p3}{}^2 + \Omega_1 \Omega_2 \Omega_3 \omega_{pe}{}^2,$

$\eta_{10} = \omega_{p1}{}^2 + \omega_{p2}{}^2 + \omega_{p3}{}^2 + \omega_{pe}{}^2,$

$N_1 = \dfrac{n\Omega_\sigma}{\gamma}, \quad N_2 = \dfrac{1}{\beta \cos\alpha \cos\theta}, \quad x = \tan(\theta),$

$\gamma = E + 1, \quad \beta = [E(E+2)]^{1/2}/(E+1), \quad E = E_k/(m_\sigma c^2).$

References

Albert, J. M. (2003), Evaluation of quasi-linear diffusion coefficients for EMIC waves in a multispecies plasma, *J. Geophys. Res.*, *108*(A6), 1249, doi:10.1029/2002JA009792.

Albert, J. M., and J. Bortnik (2009), Nonlinear interaction of radiation belt electrons with electromagnetic ion cyclotron waves, *Geophys. Res. Lett.*, *36*, L12110, doi:10.1029/2009GL038904.

Allen, R. C., et al. (2015), A statistical study of EMIC waves observed by Cluster: 1. Wave properties, *J. Geophys. Res. Space Physics*, *120*, doi:10.1002/2015JA021333.

Anderson, B. J., and D. J. Hamilton (1993), Electromagnetic ion cyclotron waves stimulated by modest magnetospheric compressions, *J. Geophys. Res.*, *98*, 11,369–11,382, doi:10.1029/93JA00605.

Anderson, B. J., R. E. Erlandson, and L. J. Zanetti (1992a), A statistical study of Pc1-2 magnetic pulsations in the equatorial magnetosphere: 1. Equatorial occurrence distributions, *J. Geophys. Res.*, *97*, 3075–3088, doi:10.1029/91JA02706.

Anderson, B. J., R. E. Erlandson, and L. J. Zanetti (1992b), A statistical study of Pc1-2 magnetic pulsations in the equatorial magnetosphere: 2. Wave properties, *J. Geophys. Res.*, *97*, 3089–3101, doi:10.1029/91JA02697.

Bräysy, T., K. Mursula, and G. Marklund (1998), Ion cyclotron waves during a great magnetic storm observed by Freja double-probe electric field instrument, *J. Geophys. Res.*, *103*, 4145–4155, doi:10.1029/97JA02820.

Chen, L., R. M. Thorne, and J. Bortnik (2011), The controlling effect of ion temperature on EMIC wave excitation and scattering, *Geophys. Res. Lett.*, *38*, L16109, doi:10.1029/2011GL048653.

Chen, L., R. M. Thorne, Y. Y. Shprits, and B. Ni (2013), An improved dispersion relation for parallel propagating electromagnetic waves in warm plasmas: Application to electron scattering, *J. Geophys. Res. Space Physics*, *118*, 2185–2195, doi:10.1002/jgra.50260.

Clilverd, M. A., C. J. Rodger, R. M. Millan, J. G. Sample, M. Kokorowski, M. P. McCarthy, T. Ulich, T. Raita, A. J. Kavanagh, and E. Spanswick (2007), Energetic particle precipitation into the middle atmosphere triggered by a coronal mass ejection, *J. Geophys. Res.*, *112*, A12206, doi:10.1029/2007JA012395.

Cornwall, J. M., F. V. Coroniti, and R. M. Thorne (1970), Turbulent loss of ring current protons, *J. Geophys. Res.*, *75*, 4699–4709, doi:10.1029/JA075i025p04699.

Engebretson, M. J., et al. (2015), Van Allen probes, NOAA, GOES, and ground observations of an intense EMIC wave event extending over 12 hours in MLT, *J. Geophys. Res. Space Physics*, *120*, doi:10.1002/2015JA021227.

Erlandson, R. E., and A. J. Ukhorskiy (2001), Observations of electromagnetic ion cyclotron waves during geomagnetic storms: Wave occurrence and pitch angle scattering, *J. Geophys. Res.*, *106*, 3883–3895, doi:10.1029/2000JA000083.

Fraser, B. J., and T. S. Nguyen (2001), Is the plasmapause a preferred source region of electromagnetic ion cyclotron waves in the magnetosphere?, *J. Atmos. Sol. Terr. Phys.*, *63*, 1225–1247.

Fraser, B. J., J. C. Samson, Y. D. Hu, R. L. McPherron, and C. T. Russell (1992), Electromagnetic ion cyclotron waves observed near the oxygen cyclotron frequency by ISEE 1 and 2, *J. Geophys. Res.*, *97*, 3063–3074, doi:10.1029/91JA02447.

Fraser, B. J., H. J. Singer, W. J. Hughes, J. R. Wygant, R. R. Anderson, and Y. D. Hu (1996), CRRES Poynting vector observations of electromagnetic ion cyclotron waves near the plasmapause, *J. Geophys. Res.*, *101*, 15,331–15,343, doi:10.1029/95JA03480.

Glauert, S. A., and R. B. Horne (2005), Calculation of pitch angle and energy diffusion coefficients with the PADIE code, *J. Geophys. Res.*, *110*, A04206, doi:10.1029/2004JA010851.

Horne, R. B., and R. M. Thorne (1994), Convective instabilities of electromagnetic ion cyclotron waves in the outer magnetosphere, *J. Geophys. Res.*, *99*, 17,259–17,273, doi:10.1029/94JA01259.

Jordanova, V. K., C. J. Farrugia, R. M. Thorne, G. V. Khazanov, G. D. Reeves, and M. F. Thomsen (2001), Modeling ring current proton precipitation by electromagnetic ion cyclotron waves during the May 14–16, 1997, storm, *J. Geophys. Res.*, *106*, 7–22, doi:10.1029/2000JA002008.

Keika, K., K. Takahashi, A. Y. Ukhorskiy, and Y. Miyoshi (2013), Global characteristics of electromagnetic ion cyclotron waves: Occurrence rate and its storm dependence, *J. Geophys. Res. Space Physics*, *118*, 4135–4150, doi:10.1002/jgra.50385.

Kennel, C. F. (1969), Consequences of a magnetospheric plasma, *Rev. Geophys.*, *7*(1, 2), 379–419, doi:10.1029/RG007i001p00379.

Kennel, C. F., and H. Petschek (1966), Limit on stably trapped particle fluxes, *J. Geophys. Res.*, *71*, 1–28, doi:10.1029/JZ071i001p00001.

Kersten, T., R. B. Horne, S. A. Glauert, N. P. Meredith, B. J. Fraser, and R. S. Grew (2014), Electron losses from the radiation belts caused by EMIC waves, *J. Geophys. Res. Space Physics*, *119*, 8820–8837, doi:10.1002/2014JA020366.

Kozyra, J. U., T. E. Cravens, A. F. Nagy, E. G. Fontheim, and R. S. B. Ong (1984), Effects of energetic heavy ions on electromagnetic ion cyclotron wave generation in the plasmapause region, *J. Geophys. Res.*, *89*, 2217–2233, doi:10.1029/JA089iA04p02217.

Lenchek, A., S. Singer, and R. Wentworth (1961), Geomagnetically trapped electrons from cosmic ray albedo neutrons, *J. Geophys. Res.*, *66*(12), 4027–4046, doi:10.1029/JZ066i012p04027.

Li, W., Y. Y. Shprits, and R. M. Thorne (2007), Dynamic evolution of energetic outer zone electrons due to wave-particle interactions during storms, *J. Geophys. Res.*, *112*, A10220, doi:10.1029/2007JA012368.

Liang, J., E. Donovan, B. Ni, C. Yue, F. Jiang, and V. Angelopoulos (2014), On an energy-latitude dispersion pattern of ion precipitation potentially associated with magnetospheric EMIC waves, *J. Geophys. Res. Space Physics*, *119*, 8137–8160, doi:10.1002/2014JA020226.

Liu, K., D. Winske, S. P. Gary, and G. D. Reeves (2012), Relativistic electron scattering by large amplitude electromagnetic ion cyclotron waves: The role of phase bunching and trapping, *J. Geophys. Res.*, *117*, A06218, doi:10.1029/2011JA017476.

Ma, Q., et al. (2015), Modeling inward diffusion and slow decay of energetic electrons in the Earth's outer radiation belt, *Geophys. Res. Lett.*, *42*, 987–995, doi:10.1002/2014GL062977.

McCollough, J. P., S. R. Elkington, and D. N. Baker (2012), The role of Shabansky orbits in compression-related electromagnetic ion cyclotron wave growth, *J. Geophys. Res.*, *117*, A01208, doi:10.1029/2011JA016948.

Meredith, N. P., R. M. Thorne, R. B. Horne, D. Summers, B. J. Fraser, and R. R. Anderson (2003), Statistical analysis of relativistic electron energies for cyclotron resonance with EMIC waves observed on CRRES, *J. Geophys. Res.*, *108*(A6), 1250, doi:10.1029/2002JA009700.

Meredith, N. P., R. B. Horne, S. A. Glauert, R. M. Thorne, D. Summers, J. M. Albert, and R. R. Anderson (2006), Energetic outer zone electron loss timescales during low geomagnetic activity, *J. Geophys. Res.*, *101*, A05212, doi:10.1029/2005JA011516.

Meredith, N. P., R. B. Horne, T. Kersten, B. J. Fraser, and R. S. Grew (2014), Global morphology and spectral properties of EMIC waves derived from CRRES observations, *J. Geophys. Res. Space Physics*, *119*, 5328–5342, doi:10.1002/2014JA020064.

Min, K. J., K. K. Lee, and W. Li (2012), Global distribution of EMIC waves derived from THEMIS observations, *J. Geophys. Res.*, *117*, A05219, doi:10.1029/2012JA017515.

Miyoshi, Y., K. Sakaguchi, K. Shiokawa, D. Evans, J. Albert, M. Connors, and V. Jordanova (2008), Precipitation of radiation belt electrons by EMIC waves, observed from ground and space, *Geophys. Res. Lett.*, *35*, L23101, doi:10.1029/2008GL035727.

Morley, S. K., S. T. Ables, M. D. Sciffer, and B. J. Fraser (2009), Multipoint observations of Pc1-2 waves in the afternoon sector, *J. Geophys. Res.*, *114*, A09205, doi:10.1029/2009JA014162.

Ni, B., R. M. Thorne, Y. Y. Shprits, and J. Bortnik (2008), Resonant scattering of plasma sheet electrons by whistler-mode chorus: Contribution to diffuse auroral precipitation, *Geophys. Res. Lett.*, *35*, L11106, doi:10.1029/2008GL034032.

Ni, B., R. M. Thorne, N. P. Meredith, R. B. Horne, and Y. Y. Shprits (2011), Resonant scattering of plasma sheet electrons leading to diffuse auroral precipitation: 2. Evaluation for whistler mode chorus waves, *J. Geophys. Res.*, *116*, A04219, doi:10.1029/2010JA016233.

Ni, B., J. Liang, R. M. Thorne, V. Angelopoulos, R. B. Horne, M. Kubyshkina, E. Spanswick, E. F. Donovan, and D. Lummerzheim (2012), Efficient diffuse auroral electron scattering by electrostatic electron cyclotron harmonic waves in the outer magnetosphere: A detailed case study, *J. Geophys. Res.*, *117*, A01218, doi:10.1029/2011JA017095.

Ni, B., J. Bortnik, R. M. Thorne, Q. Ma, and L. Chen (2013), Resonant scattering and resultant pitch angle evolution of relativistic electrons by plasmaspheric hiss, *J. Geophys. Res. Space Physics*, *118*, 7740–7751, doi:10.1002/2013JA019260.

Ni, B., et al. (2014a), Resonant scattering of energetic electrons by unusual low-frequency hiss, *Geophys. Res. Lett.*, *41*, 1854–1861, doi:10.1002/2014GL059389.

Ni, B., J. Bortnik, Y. Nishimura, R. M. Thorne, W. Li, V. Angelopoulos, Y. Ebihara, and A. T. Weatherwax (2014b), Chorus wave scattering responsible for the Earth's dayside diffuse auroral precipitation: A detailed case study, *J. Geophys. Res. Space Physics*, *19*, 897–908, doi:10.1002/2013JA019507.

Pickett, J. S., et al. (2010), Cluster observations of EMIC triggered emissions in association with Pc1 waves near Earth's plasmapause, *Geophys. Res. Lett.*, *37*, L09104, doi:10.1029/2010GL042648.

Reeves, G. D., K. L. McAdams, R. H. W. Friedel, and T. P. O'Brien (2003), Acceleration and loss of relativistic electrons during geomagnetic storms, *Geophys. Res. Lett.*, *30*(10), 1529, doi:10.1029/2002GL016513.

Rodger, C. J., T. Raita, M. A. Clilverd, A. Seppälä, S. Dietrich, N. R. Thomson, and T. Ulich (2008), Observations of relativistic electron precipitation from the radiation belts driven by EMIC waves, *Geophys. Res. Lett.*, *35*, L16106, doi:10.1029/2008GL034804.

Roederer, J. G. (1970), *Dynamics of Geomagnetically Trapped Radiation*, Springer, New York.

Schulz, M. (1974), Particle lifetimes in strong diffusion, *Astrophys. Space Sci.*, *31*, 37–42.

Sheeley, B. W., M. B. Moldwin, H. K. Rassoul, and R. R. Anderson (2001), An empirical plasmasphere and trough density model: CRRES observations, *J. Geophys. Res.*, *106*, 25,631–25,641, doi:10.1029/2000JA000286.

Shprits, Y. Y., and B. Ni (2009), Dependence of the quasi-linear scattering rates on the wave normal distribution of chorus waves, *J. Geophys. Res.*, *114*, A11205, doi:10.1029/2009JA014223.

Silin, I., I. R. Mann, R. D. Sydora, D. Summers, and R. L. Mace (2011), Warm plasma effects on electromagnetic ion cyclotron wave MeV electron interactions in the magnetosphere, *J. Geophys. Res.*, *116*, A05215, doi:10.1029/2010JA016398.

Stix, T. H. (1962), The Theory of Plasma Waves, McGraw-Hill, New York.

Subbotin, D., Y. Shprits, and B. Ni (2010), Three-dimensional VERB radiation belt simulations including mixed diffusion, *J. Geophys. Res.*, *115*, A03205, doi:10.1029/2009JA015070.

Summers, D. (2005), Quasi-linear diffusion coefficients for field-aligned electromagnetic waves with applications to the magnetosphere, *J. Geophys. Res.*, *110*, A08213, doi:10.1029/2005JA011159.

Summers, D., and R. M. Thorne (2003), Relativistic electron pitch angle scattering by electromagnetic ion cyclotron waves during geomagnetic storms, *J. Geophys. Res.*, *108*(A4), 1143, doi:10.1029/2002JA009489.

Summers, D., B. Ni, and N. P. Meredith (2007), Timescales for radiation belt electron acceleration and loss due to resonant wave-particle interactions: 2. Evaluation for VLF chorus, ELF hiss, and electromagnetic ion cyclotron waves, *J. Geophys. Res.*, *112*, A04207, doi:10.1029/2006JA011993.

Thorne, R. M., and R. Horne (1992), The contribution of ion-cyclotron waves to electron heating and SAR-arc excitation near the stormtime plasmapause, *Geophys. Res. Lett.*, *19*, 417–420, doi:10.1029/92GL00089.

Thorne, R. M., and R. Horne (1997), Modulation of electromagnetic ion cyclotron instability due to interaction with ring current O+ during magnetic storms, *J. Geophys. Res.*, *102*(A7), 14,155–14,163, doi:10.1029/96JA04019.

Thorne, R. M., and C. F. Kennel (1971), Relativistic electron precipitation during magnetic storm main phase, *J. Geophys. Res.*, *76*(19), 4446–4453, doi:10.1029/JA076i019p04446.

Thorne, R. M., et al. (2013), Evolution and slow decay of an unusual narrow ring of relativistic electrons near L~3.2 following the September 2012 magnetic storm, *Geophys. Res. Lett.*, *40*, 3507–3511, doi:10.1002/grl.50627.

Turner, D. L., et al. (2014a), On the cause and extent of outer radiation belt losses during the 30 September 2012 dropout event, *J. Geophys. Res. Space Physics*, *119*, 1530–1540, doi:10.1002/2013JA019446.

Turner, D. L., et al. (2014b), Competing source and loss mechanisms due to wave-particle interactions in Earth's outer radiation belt during the 30 September to 3 october 2012 geomagnetic storm, *J. Geophys. Res. Space Physics*, *119*, 1960–1979, doi:10.1002/2014JA019770.

Ukhorskiy, A. Y., Y. Y. Shprits, B. J. Anderson, K. Takahashi, and R. M. Thorne (2010), Rapid scattering of radiation belt electrons by storm-time EMIC waves, *Geophys. Res. Lett.*, *37*, L09101, doi:10.1029/2010GL042906.

Usanova, M. E., I. R. Mann, I. J. Rae, Z. C. Kale, V. Angelopoulos, J. W. Bonnell, K.-H. Glassmeier, H. U. Auster, and H. J. Singer (2008), Multipoint observations of magnetospheric compression-related EMIC Pc1 waves by THEMIS and CARISMA, *Geophys. Res. Lett.*, *35*, L17S25, doi:10.1029/2008GL034458.

Usanova, M. E., I. R. Mann, J. Bortnik, L. Shao, and V. Angelopoulos (2012), THEMIS observations of electromagnetic ion cyclotron wave occurrence: Dependence on AE, SYMH, and solar wind dynamic pressure, *J. Geophys. Res.*, *117*, A10218, doi:10.1029/2012JA018049.

Usanova, M. E., et al. (2014), Effect of EMIC waves on relativistic and ultrarelativistic electron populations: Ground-based and Van Allen Probes observations, *Geophys. Res. Lett.*, *41*, 1375–1381, doi:10.1002/2013GL059024.

Yu, X., Z. Yuan, D. Wang, H. Li, S. Huang, Z. Wang, Q. Zheng, M. Zhou, C. A. Kletzing, and J. R. Wygant (2015), In situ observations of EMIC waves in O+ band by the Van Allen Probe A, *Geophys. Res. Lett.*, *42*, 1312–1317, doi:10.1002/2015GL063250.

Zhang, J.-C., L. M. Kistler, C. G. Mouikis, M. W. Dumlop, B. Klecker, and J.-A. Sauvaud (2010), A case study of EMIC wave-associated He+ energization in the outer magnetosphere: Cluster and Double Star 1 observations, *J. Geophys. Res.*, *115*, A06212, doi:10.1029/2009JA014784.

Zhang, J.-C., L. M. Kistler, C. G. Mouikis, B. Klecker, J.-A. Sauvaud, and M. W. Dumlop (2011), A statistical study of EMIC wave-associated He+ energization in the outer magnetosphere: Cluster/CODIF observations, *J. Geophys. Res.*, *116*, A11201, doi:10.1029/2011JA016690.

Zhang, J.-C., et al. (2014), Excitation of EMIC waves detected by the Van Allen Probes on 28 April 2013, *Geophys. Res. Lett.*, *41*, 4101–4108, doi:10.1002/2014GL060621.